Marine Research
of the National Academy of Marine Research
ISSN: 2709-6629 (Vol.3 Iss.2)
GPN: 2011200033

DOI: http://dx.doi.org/10.29677/MR.202312_3(2).0005
2023, 3(2), 60-74

Numerical Study on the Evolution of Internal and Surface Waves Propagating over a Permeable Trapezoidal Obstacle

Ming-Hung Cheng [1*] Chih-Min Hsieh [2] Robert R. Hwang [3,4]

[1] *Marine Industry and Engineering Research Center, National Academy of Marine Research, Kaohsiung City, Taiwan*
[2] *Department of Maritime Information and Technology, National Kaohsiung University of Science and Technology, Kaohsiung City, Taiwan*
[3] *Department of System Engineering and Naval Architecture, National Taiwan Ocean University, Keelung City, Taiwan*
[4] *Institute of Physics, Academia Sinica, Nankang, Taipei City, Taiwan*

ABSTRACT

Although interesting phenomena associated with the interactions between internal waves (IWs) and surface waves (SWs) over impermeable submerged obstacles have been observed in laboratory experiments and numerical models, less research has explored the effects of permeable beds on wave evolution. In this study, we employed a numerical model to solve the Navier-Stokes equations using the Improved Delayed Detached Eddy Simulation (IDDES) model for turbulence closure, investigating the evolution of internal and surface waves propagating over a permeable trapezoidal obstacle. The porous media equation was adopted to further explore the evolution of the flow field during this process. A plunger-type wavemaker was utilized to create surface pressure differences, generating both surface and internal waves. Additionally, air, water, and brine were used to simulate the complete process. The numerical simulations revealed that the amplitude and wave period of SWs are affected by the propagation of IWs over submerged obstacles. While both SWs and IWs propagate over the trapezoidal obstacle, the wave amplitude decreases significantly, but the fundamental frequency remains constant, regardless of whether the obstacle is impermeable or permeable. In the case of the impermeable obstacle, the strength of the fundamental wave period of IWs decreases as IWs propagate over the plateau. In the case of the permeable obstacle, porous effects cause the amplitude and strength of the fundamental frequency of both SWs and IWs to decrease significantly during this process. Based on the numerical simulations, the interaction mechanisms between these two waves and obstacles have been elucidated, providing essential insights for future coastal and ocean engineering endeavors.

Keywords: Internal waves, surface waves, permeable trapezoidal obstacle, wave-obstacle interaction, numerical simulations.

* Corresponding author, E-mail: chengminghung@gmail.com

Received 23 August 2023, Accepted 11 October 2023.

1 INTRODUCTION

Barotropic waves on the ocean surface (surface waves; SWs) are generated by external forces in stratified fluids. Simultaneously, baroclinic waves form at the interface (internal waves; IWs) due to different pressure variations. Field observations indicate the coexistence of IWs and SWs in oceans and estuaries. In oceans, IWs result from the interaction between tidal flows and submerged topography, while in estuaries, IWs are produced through the interaction between waves and flows. IWs, generated by surface pressure variations in oceans or estuaries, can influence stratified fluid mixing, SW transmission, bottom nutrient pumping, and lakeside scouring. Consequently, they play a significant role in ocean ecology, environmental dynamics, and coastal engineering, particularly when propagating over diverse topography (Chen et al., 2023; Das et al., 2018; McMullen et al., 2015; Trowbridge & Traykovski, 2015; Zhang and Li, 2022). For example, Ho et al. (2009) utilized the Moderate Resolution Imaging Spectroradiometer (MODIS) to observe the interaction between IWs and SWs near the Dongsha Atoll in the South China Sea (SCS). The diagrams (Figure 1), with a spatial resolution of 250 m, displayed one depression and two elevation internal wave packets on the eastern and western sides of the Dongsha Atoll, respectively. They suggested that depression-type IWs could roughen the sea surface, leading to reduced sunlight reflection captured by satellite sensors. In contrast, elevation-type IWs in the shelf area appear brighter due to the higher reflectance of sunlight on the sea surface (Ho et al., 2009).

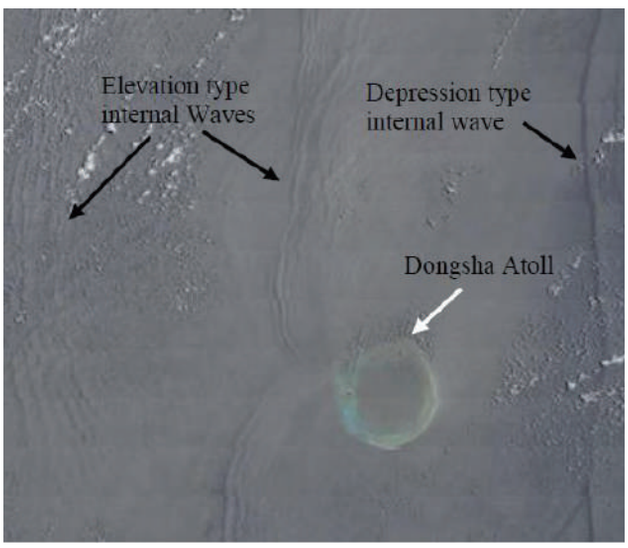

Figure 1. MODIS image showing three internal wave packets near the Dongsha Atoll. (Ho et al., 2009)

Until now, existing literature on the interaction between surface and internal waves, particularly in the presence of permeable obstacles, remains limited and unclear. Despite sequential data obtained through instruments such as acoustic Doppler current profilers (ADCPs) or conductivity, temperature, and depth (CTD) sensors in field observations, analyzing the interaction between IWs and SWs, especially over permeable topography, remains challenging. In laboratory experiments, various wave-making mechanisms have been employed to generate SWs, internal solitary waves (ISWs), or IWs. Dalziel et al. (2007) used a gate-type wavemaker to explore the transformation of ISWs on flat bottoms. Ko and Cho (2017) utilized a plunger-type wavemaker to observe interactions between SWs and IWs on flat surfaces. In terms of numerical simulations, Hsieh et al. (2019) combined laboratory experiments with numerical simulations to investigate the interaction between IWs and SWs over an impermeable slope-shelf. Hao et al. (2022) introduced a novel method for simulating complex surface waves interacting with large-amplitude internal solitary waves. Their results demonstrated that the initial wave energy growth rate of the resonant wave component aligned with the

DOI: 10.29677/MR.202312_3(2).0005

analytical value predicted by perturbation theory. They also employed this model to simulate the interaction between SWs and weakly nonlinear IWs, with results nearly identical to those calculated using a two-layer model. Furthermore, Zhang et al. (2023) examined the simplification strategy of retaining only the nonhydrostatic effect of local acceleration in a three-dimensional fully nonhydrostatic model concerning submesoscale wave phenomena in the ocean.

In this study, numerical simulations were conducted to investigate the variations in waveform and wave frequency as IWs and SWs propagated over a permeable trapezoidal obstacle. The simulations took place in a stratified fluid system within a steel-framed wave tank measuring 12 meters in length, 0.7 meters in height, and 0.5 meters in width. The fluid density of the upper and bottom layers was set at 996 and 1030 kg/m³, respectively. A vertically removable plunger-type wave maker was installed on the right-hand side of the tank to generate SWs and induce IWs. The porosity ratios used in this study were 0 and 0.49, respectively. By analyzing the measured data and employing the Hilbert-Huang Transform (HHT) method for frequency analysis, the spatiotemporal variations of waveforms during this process were examined. The results obtained from impermeable and permeable numerical simulations were utilized to study the spatiotemporal evolutions of isopycnic waveforms and flow fields throughout the process. Through these numerical simulations, the mechanism of interaction between the two waves and the obstacle can be clearly understood, providing valuable insights for future coastal and ocean engineering endeavors.

2 NUMERICAL METHODOLOGY

In this study, the general mass continuity equation, the conservation of momentum, and the transport equation are written as follows:

$$\frac{\partial \overline{u}_i}{\partial x_i} = 0 \tag{1}$$

$$\frac{\partial \overline{u}_i}{\partial t} + \frac{\partial}{\partial x_j}\left(\overline{u}_i\,\overline{u}_j\right) = -\frac{1}{\rho}\frac{\partial \overline{P}}{\partial x_i} + \frac{1}{\rho}\frac{\partial \tau_{ij}^R}{\partial x_j} + \upsilon\nabla^2\overline{u}_i + g_i\frac{\Delta\rho}{\rho} \tag{2}$$

$$\frac{\partial \alpha_i}{\partial t} + \nabla\cdot\left(\phi_{\alpha_i}\right) = \nabla\cdot D_{ij}(\nabla\alpha_i) + S_{\alpha_i} \tag{3}$$

where $\overline{u}_i$ denotes the mean velocity components (U, W) in a 2D Cartesian coordinate system (x, z), respectively; u_i is the velocity components ($=\overline{u}_i + u_i'$); t the time; $\Delta\rho$ the difference of fluid density ($\rho - \rho_0$; ρ_0 is the density in the upper layer; ρ is the fluid density varied along with y-label); P the dynamic pressure; v is the kinematic viscosity; D_{ij} is the molecular diffusivity between two fluids (as the two fluids are not mixing, the value is zero); α_i means the volume occupancy of the fluis; and S_{α_i} is the value of volumetric source. Item τ_{ij}^R ($= \rho\left(\overline{u_i u_j} - \overline{u}_i\,\overline{u}_j\right)$) is the subgrid-stress tensor, which includes the residual stress; $-\overline{u_i'\rho'}$ ($= \frac{\upsilon_t}{S_{ct}}\frac{\partial \rho}{\partial x_i}$) is the mean turbulent fluxes of the mean density ρ; g_i ($= [0, -g]$) is the gravitational acceleration. S_{ct} is the turbulent Schmidt number ($= \nu_t/D_K$), in which D_K is the eddy diffusivity. The overbar (-) indicates the averaging of fluctuating quantities. An Eddy-viscosity model can be defined unresolved in LES and written as:

$$\tau_{ij}^R - \frac{1}{3}\delta_{ij}\tau_{kk}^R = -2\rho\upsilon_t\overline{s}_{ij} \tag{4}$$

where ν_t is the turbulent viscosity; $\overline{s}_{ij} = \left(\frac{\partial \overline{u}_i}{\partial x_j} + \frac{\partial \overline{u}_j}{\partial x_i}\right)$; δ_{ij} is the Kronecker delta. The Eq. (2) can be written as:

$$\frac{\partial \overline{u}_i}{\partial t} + \frac{\partial}{\partial x_j}\left(\overline{u}_i\,\overline{u}_j\right) = -\frac{1}{\rho}\frac{\partial \overline{P}}{\partial x_i} + 2\frac{\partial}{\partial x_j}(\upsilon + \upsilon_t)\overline{s}_{ij} + g_i\frac{\Delta\rho}{\rho} \tag{5}$$

Marine Research of the National Academy of Marine Research
DOI: 10.29677/MR.202312_3(2).0005

The hybrid IDDES method with Spalart-Allmaras RANS is adopted to determine the turbulent viscosity (v_t). The turbulent eddy viscosity can be calculated with $\upsilon_t = f_{v1}\tilde{\upsilon}$, where $f_{v1} = \frac{\chi^3}{\chi^3 + C_{v1}^3}$, $\chi = \frac{\tilde{\upsilon}}{\upsilon}$. The transport equation for the modified Kinematic eddy viscosity $\tilde{\upsilon}$ can be written as:

$$\frac{\partial \tilde{\upsilon}}{\partial t} + \frac{\partial}{\partial x_i}(\tilde{\upsilon} u_i) = \frac{1}{C_\sigma}\left\{\frac{\partial}{\partial x_i}[\upsilon + \tilde{\upsilon}]\nabla\tilde{\upsilon} + C_{b2}\frac{\partial \tilde{\upsilon}}{\partial x_i}\frac{\partial \tilde{\upsilon}}{\partial x_j}\right\} + C_{b1}\tilde{S}\tilde{\upsilon} - C_{\omega 1} f_\omega \left(\frac{\tilde{\upsilon}}{\tilde{d}}\right)^2 \tag{6}$$

where

$$\tilde{S} = \omega + f_{v2}\frac{\tilde{\upsilon}}{(\kappa \tilde{d})^2};\ f_{v2} = 1 - \frac{\chi}{1 + f_{v1}\chi} \tag{7}$$

$$f_\omega = g_t * \left(\frac{1 + C_{\omega 1}^6}{g_t + C_{\omega 3}^6}\right)^{1/6};\ g_t = \gamma + C_{\omega 2}(\gamma^6 - \gamma);\ \gamma = \frac{\tilde{\upsilon}}{\tilde{s}(\kappa \tilde{d})^2} \tag{8}$$

The adopted parameter values are: C_σ= 2/3, C_{b1} = 0.1355, C_{b2} = 0.622, C_{v1} = 7.1, $C_{\omega 1}$ = (C_{b1} / κ^2+ (1+C_{b2}) / C_σ), $C_{\omega 2}$ = 0.3, $C_{\omega 3}$ = 2, κ = 0.41. The IDDES model is defined by Shur et al. (2008) and a new turbulent length scale is adopted and defined as:

$$\tilde{d} = \tilde{f}_d * (1 + f_e) * l_{RANS} + \left(1 - \tilde{f}_d\right) * l_{LES} \tag{9}$$

where $l_{RANS} = d_w$, $l_{LES} = C_{DES} * \psi * \Delta$.

$$\Delta = \min\{max[C_w d_w, C_w \Delta_{max,} \Delta_{wn}], \Delta_{max,}\};$$

$$\tilde{f}_d = max[(1 - f_{dt}), f_B];\ f_{dt} = 1 - tanh[(8\tau_{dt})^3];\ f_B = min[2cxp(-9\alpha^2), 1];\ \alpha = 0.25 - \frac{d_w}{h_{max}};$$

$$f_e = max[(f_{e1} - 1), 0] * \psi * f_{e2};\ f_{e1} = \{2exp(-11.09\alpha^2)\ if\ \alpha \geq 0 | 2exp(-9\alpha^2)\ if\ \alpha < 0\};$$

$$f_{e2} = 1 - max(f_t, f_l);\ f_t = tanh[(C_t^2 \tau_{dt})^3];$$

$$f_l = tanh[(C_l^2 \tau_{dl})^{10}];$$

$$\tau_{dt} = \frac{\upsilon_t}{(\kappa d_w)^2 * max\left(\left[\sum_{ij}\left(\frac{\partial u_i}{\partial x_i}\right)^2\right]^{1/2}, 10^{-10}\right\}};$$

$$\tau_{dl} = \frac{\upsilon}{(\kappa d_w)^2 * max\left(\left[\sum_{ij}\left(\frac{\partial u_i}{\partial x_i}\right)^2\right]^{1/2}, 10^{-10}\right\}};$$

$$\psi^2 = min\left\{10^2, \frac{1 - \frac{C_{b1}}{C_{w1}\kappa^2 f_\omega^*}[f_{t2} + (1 - f_{t2})f_{v2}]}{f_{v1} max(10^{-10}, 1 - f_{t2})}\right\};$$

d_w represents the distance to the wall; Δ_{wn} is the grid step in the wall normal direction; the parameters of C_l, C_t, C_w, and f_w^* are 3.55, 1.63, 0.15 and 0.424, respectively (Cheng et al., 2020).

As the submerged obstacle is permeable, the Darcy-Forchheimer function was adopted to calculate the inertial force term and viscous force term of the permeable flow in this study. Subsequently, the Eqs. (3) and (5) were re-written as:

Marine Research of the National Academy of Marine Research
DOI: 10.29677/MR.202312_3(2).0005

$$\frac{\partial \overline{u}_i}{\partial t} + \frac{1}{n_f}\frac{\partial}{\partial x_j}\left(\overline{u}_i\,\overline{u}_j\right) = -\frac{n_f}{\rho}\frac{\partial \overline{P}}{\partial x_i} + 2\frac{\partial}{\partial x_j}(\upsilon + \upsilon_t)\overline{s}_{ij} + n_f g_i \frac{\Delta\rho}{\rho} + F_d \tag{10}$$

$$\frac{\partial \alpha_i}{\partial t} + \frac{1}{n_f}\nabla\cdot\left(\phi_{\alpha_i}\right) = \nabla\cdot D_{ij}(\nabla\alpha_i) + S_{\alpha_i} \tag{11}$$

where n_f is the porosity ratio; F_d means the forcing term in the Reynolds number dependent porous model and is given by Eq. (12),

$$F_d = -150\frac{(1-n_f)^3}{n_f^3}\frac{\nu}{D_{50}^2}\overline{u}_i - 0.875\frac{\overline{u}_i|\overline{u}_i|(1-n_f)}{D_{50}n_f^3} \tag{12}$$

where n_f is the porosity, D_{50} is the mean size of the sandy sediment.

For this study, numerical experiments were conducted to examine propagation of SWs and IWs in a stratified fluid system inside a steel-framed wave tank, which was 12 m long with a cross section 0.7 m high by 0.5 m wide (Figure 1). The trapezoidal obstacle had a height of 0.37 m (h_s) above the bottom of the flume and was connected to a front slope of θ = 13°. The middle ridge was 6.8 m of the flume. The total water depth including the upper (H_1 = 0.12 m) and bottom (H_2 = 0.38 m) layers was 0.50 m. Fluid density of the upper and bottom layer was 996 and 1,030 kg/m3, respectively. A vertically removable plunger type wave-maker (quarter cylindrical shape; R_s = 0.16 m) was mounted on the right-hand side of the tank to generate IWs. The numerical sponge layer was utilized to prevent secondary wave reflections. Wave absorbers were installed at the upstream and downstream ends of the tank to absorb the transmitted wave energy over the submerged obstacle. The porosity ratio was 0 and 0.49, respectively. Three numerical probes were utilized to capture the waveforms of IWs and SWs at specific locations as indicated in Figure 2. For this study, the wave maker exclusively interacted with the free surface by moving up and down, without making direct contact with the interface; the lowest position of the wave maker was 0.05 m above the interface, generating continuous surface waves. As these surface waves propagated, varying surface pressures indirectly affected the interface, resulting in periodic IWs. In this setup, the wave height and period of IWs are influenced by the bottom depth and the conditions of the SWs. However, the phase and period of the IWs may not necessarily synchronize with those of the SWs. The wave maker operated at a speed of P_s = 40 rps, with a repeated period of approximately 4.5s. A long incident wave period was employed to generate nonlinear continuous IWs and SWs, enabling the exploration of the impact of wave periods. Based on this method, nonlinear continuous waveforms were generated. The time-frequency analysis was conducted using the Hilbert-Huang Transform (HHT; Huang et al., 1998) method to determine the major wave frequencies of SWs and IWs during this process.

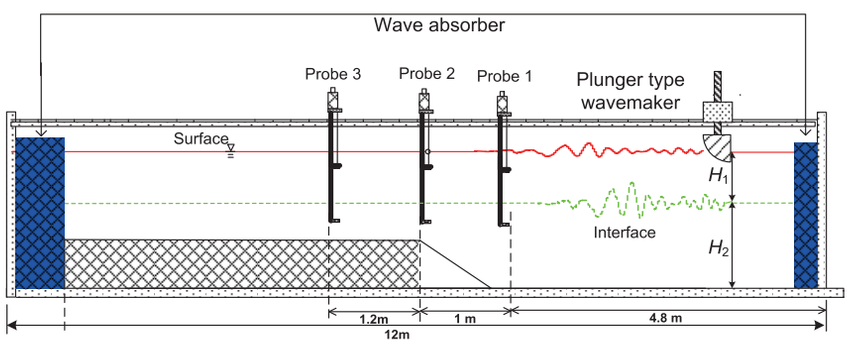

Figure 2. Schematic diagram showing IWs and SWs propagating over a submerged ridge. (Not to scale)

The HHT approach utilizes an empirical mode decomposition (EMD) method and Hilbert spectral analysis. In the EMD component, an original wave profile data $\eta(t)$ is decomposed into several intrinsic mode functions (IMFs), such that,

DOI: 10.29677/MR.202312_3(2).0005

$$\eta(t) = \Sigma^{n}_{j=1} C_j(t) + r_{n+1}(t) \quad (13)$$

where C_j is an IMF, r_{n+1} is the residue (or "trend") embedded in the original time series $\eta(t)$ after n lots of IMFs being numerically extracted. Each of the IMF is a simple oscillatory function with a specific wave height and frequency (or period) and has unique properties regarding the number of local extrema and the zero-crossing points, as well as zero mean value of the envelope bounded by the local maxima and minima. Once the IMFs are calculated numerically from the laboratory data, the results are then used to produce a Hilbert spectrum (Eq. 13) which indicates the variations in the instantaneous wave height ($a_j(t)$) and wave frequency ($\omega_j(t)$) as a function of time embedded in the wave record.

$$A(\omega,t) = \mathrm{Real}\Sigma^{n}_{j=1} a_j(t) \exp(i \int \omega_j(t)\mathrm{d}t) \quad (14)$$

After applying the aforementioned method, a time series of the IMFs profiles is utilized to calculate the Hilbert spectrum, which represents time-period-energy patterns. The output is akin to that obtained from wavelet analysis. Additionally, the marginal spectrum is computed, resembling the conventional energy spectrum generated by the fast Fourier transform (FFT) algorithm. The conventional energy spectrum provides the overall energy distribution, but does not capture specific time instances when particular wave conditions were present. In the next section, we present the results, including waveforms, and wave frequency, obtained from the aforementioned method, and discuss them in detail.

3 NUMERICAL RESULTS

The spatiotemporal evolutions of SWs and IWs at two different porosity ratios are presented and the effect of a porous obstacle is discussed in this section. The waveform evolutions of SWs and IWs are found to be insignificant under weak and moderate IWs-topography interactions; hence, only the case of strong breaking is considered in this paper. A slow wave maker speed (i.e., P_s = 40 rps) is employed to study the transmission effects of SWs and IWs.

3.1 Spatiotemporal Evolutions of Density and Flow Field

Based on the previous numerical simulations, the spatiotemporal results of isopycnic patterns with flow field when SWs and ISWs propagate over impermeable and permeable trapezoidal obstacles are illustrated in Figure 3, respectively. The colormap represents the magnitude of isopycnic patterns, and the air layer is depicted in white. This diagram depicts the results of a wave period, and shows two waves generated using a plunger wavemaker in the surface layer. Firstly, the leading crest of IWs propagates significantly along the shoulder of an impermeable trapezoidal obstacle (Figure 3a1). The negative horizontal velocity occurs due to the interaction between the leading trough of IWs and the obstacle. Both horizontal and vertical velocities increase significantly when IWs encounter the front slope of the impermeable obstacle, owing to the narrow space between IWs and the bottom. Concurrently, the waveform of SWs weakens due to the strong IW-obstacle interaction. As the leading trough of IWs passes over the shoulder and onto the plateau of the trapezoidal obstacle (Figure 3a2), a significant SWs waveform is observed in the surface layer because of the weak IW-obstacle interaction. Similar phenomena of SWs and IWs propagating over an impermeable trapezoidal obstacle occur again due to the periodic nature of waves. Although the process of IWs propagating over a trapezoidal obstacle resembles that of an Internal Solitary Wave (ISW), a weak internal hydraulic jump is generated in the former case. This is because the IWs have similar wavelengths for troughs and crests. However, the interaction time between the trough of IWs and the obstacle is too short to generate a complete internal hydraulic jump, as observed when IWs propagate over a submerged obstacle.

Marine Research of the National Academy of Marine Research
DOI: 10.29677/MR.202312_3(2).0005

Figure 3b1-3b2 illustrate the spatiotemporal progressions of isopycnic patterns and the flow field when dealing with a permeable submerged obstacle. A comparison between the impermeable and permeable obstacles reveals a notable weakening of the leading crest of SWs and IWs during the wave-obstacle interaction, both on the shoulder and plateau. Although the leading crest and trough of IWs propagate over the submerged trapezoidal obstacle (Figure 3b1-3b2), the internal hydraulic jump induced by the interaction between the IW trough and the obstacle becomes substantially weaker. Additionally, there is no significant increase in horizontal and vertical velocities as IWs encounter the front slope of the permeable obstacle, where the space between IWs and the bottom narrows. This is because the permeable obstacle allows water to pass through its interior. Furthermore, the amplitude of IWs decreases due to the interaction with the porous obstacle. Consequently, the weak IW-obstacle interaction also minimizes its impact on the evolution of SWs. In summary, the presence of a permeable obstacle leads to a reduction in both IWs and SWs as waves propagate over a trapezoidal obstacle. Moreover, the internal hydraulic jump is significantly diminished due to the weak interaction.

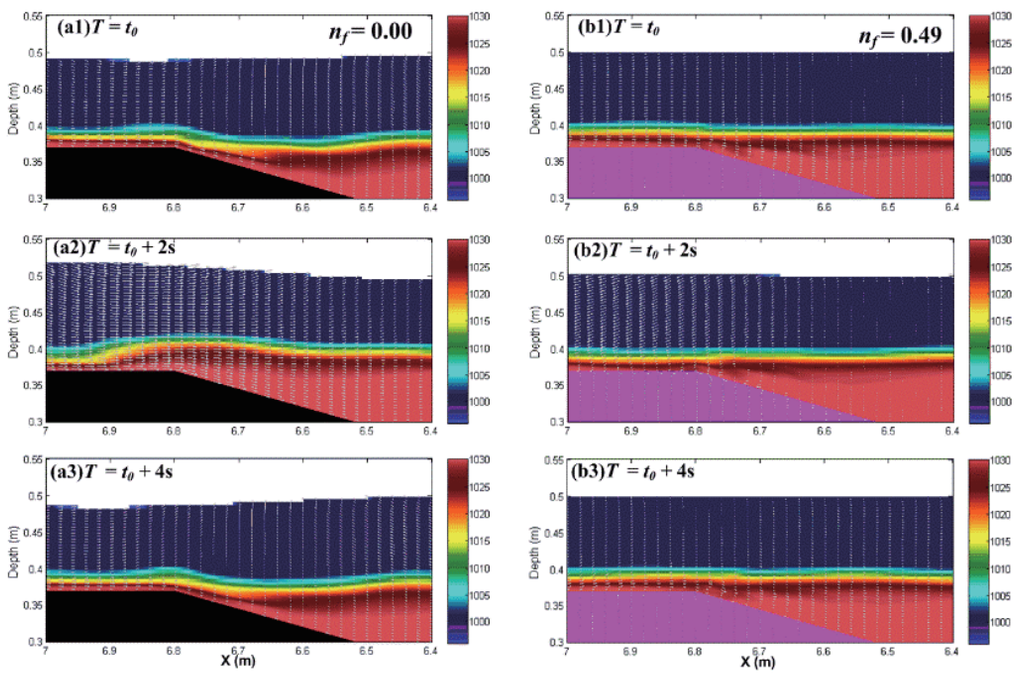

Figure 3. Numerical results for spatiotemporal variations in isopycnic contours for the flow field with porosity n_f = 0 and 0.49, respectively. (The parts in pink indicate the boundary of the trapezoidal obstacle in kgm^{-3})

3.2 Temporal Evolutions of SWs and IWs

The previous section outlined the spatial evolution of isopycnic patterns and the flow field. The temporal evolutions of SWs and IWs are shown in Figure 4 and 5, respectively. Based on these temporal variations, the influence of porosity on both SWs and IWs propagating over a trapezoidal obstacle can be clearly discussed in this section. Figure 4 illustrates the waveforms of SWs recorded by three numerical probes at impermeable and permeable obstacles, respectively. Comparing the two cases, the amplitude of SWs at the impermeable obstacle (Figure 4a1-a3) is larger than that at the permeable obstacle (Figure 4b1-b3). As the IWs encounter the front slope of the trapezoidal obstacle, strong IWs-obstacle interactions reoccur. Consequently, the amplitude of SWs recorded by Probe 2 at the impermeable obstacle significantly increases. However, the same amplitude of SWs

Marine Research of the National Academy of Marine Research
DOI: 10.29677/MR.202312_3(2).0005

recorded by Probe 1 and Probe 2 is observed at the permeable obstacle due to weak IWs-obstacle interactions. When the SWs pass through the shoulder and on the plateau, the amplitude of transmitted SWs decreases only weakly at the impermeable obstacle due to strong IWs-obstacle interactions (Figure 4a3). In contrast, the amplitude decreases significantly at the permeable obstacle because of weak wave-obstacle interactions (Figure 4b3). Furthermore, the complex waveform at Probe 2 becomes smooth as the SWs propagate over the impermeable obstacle (Figure 4a2-a3). This is because the strong IWs-obstacle interactions cause the complex waveform of SWs at Probe 2, while the influence of IWs at Probe 3 weakens on the plateau. In the case of the permeable obstacle, the waveform of SWs at Probe 2 is not affected by the internal hydraulic jump and strong IWs-obstacle interactions. Hence, the amplitude of SWs does not significantly increase. As the SWs propagate on the plateau, only the transmitted decay of SWs is investigated.

Figure 5 displays the temporal waveforms of IWs recorded by three numerical probes at impermeable and permeable obstacles, respectively. Based on the results, the initial waveform of IWs in both cases is similar (Figure 5a1 and b1) due to the same wave generation. As the IWs propagate on the front slope of the trapezoidal obstacle, the waveform of IWs at the impermeable obstacle is larger than that at the permeable obstacle (Figure 5a2 and b2). This difference arises because the impermeable obstacle induces an internal hydraulic jump, increasing the waveform of IWs, while the porous obstacle allows wave infiltration, decreasing the amplitude of IWs. The transmitted amplitude of IWs significantly decreases as the IWs propagate on the plateau, whether the obstacle is impermeable or permeable (Figure 5a3 and b3). In the case of the impermeable obstacle, this decay is due to the strong interaction between IWs and the front slope. In the case of the permeable obstacle, the decrease occurs due to the infiltrative effect. Comparing SWs and IWs, the amplitude of SWs is larger than that of IWs during this process. Furthermore, in the case of the impermeable obstacle, the waveform of SWs is significantly affected by the IWs, especially at the front slope. The IWs exert a wake influence on the transmitted SWs when the obstacle is impermeable. On the other hand, the porous effect causes a significant decrease in the transmitted IWs, making the transmitted IWs primarily induced by water viscosity.

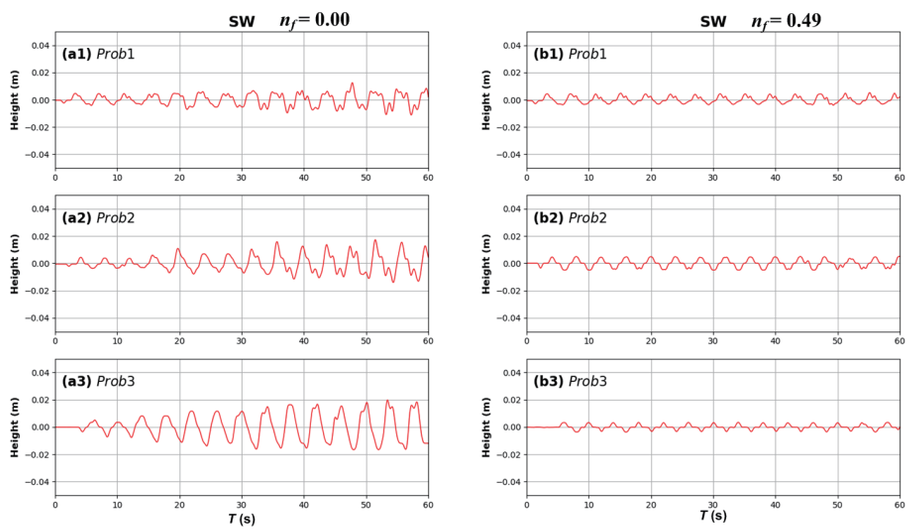

Figure 4. Numerical results of surface waves at impermeable and permeable obstacles. (Exp.: H_1 = 0.12 m, H_2 = 0.38 m, P_s = 40 rps)

Marine Research of the National Academy of Marine Research
DOI: 10.29677/MR.202312_3(2).0005

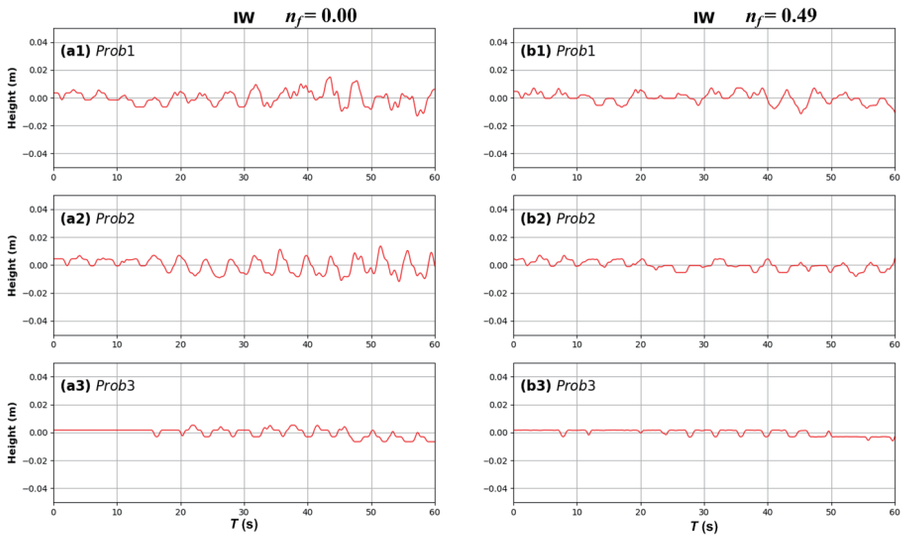

Figure 5. Numerical results of internal waves at impermeable and permeable obstacles. (Exp.: H_1 = 0.12 m, H_2 = 0.38 m, P_s = 40 rps)

The Hilbert spectrum calculated by three numerical probes of SWs and IWs at impermeable and permeable obstacles is depicted in Figure 6 and 7, respectively. The magnitude of wave energy is indicated by the color bar. In Figure 6, it can be observed that the transmitted wave energy of SWs in impermeable obstacles is larger than that in permeable ones. Regardless of whether the obstacle is impermeable or permeable, a single fundamental frequency (i.e., the wave period of the strongest internal wave energy) of SWs can be identified as the waves propagate over the trapezoidal obstacle. If it is impermeable, the transmitted wave energy of SWs significantly increases as the SWs and IWs propagate on the front slope of the trapezoidal obstacle (Figure 6a1-6a3) due to strong IWs-obstacle interactions; if it is permeable, the transmitted wave energy of SWs only weakly decreases due to water viscosity (Figure 6b1-6b3). Moreover, complex oscillations of wave frequency can occur as SWs propagate on the front slope of the trapezoidal obstacle (Figure 6a2) due to the internal hydraulic jump and IWs-obstacle interactions. In impermeable obstacles, these frequency oscillations are also observed due to SWs with a large amplitude (Figure 6a3). In permeable obstacles, porous interactions lead to small amplitude of SWs, resulting in weaker total wave energy than in impermeable obstacles. Furthermore, oscillations of wave frequency are also present as SWs propagate over the front slope of a trapezoidal obstacle (Figure 6b2). When the SWs propagate on the plateau, these frequency oscillations dissipate significantly due to the small amplitude of SWs.

The Hilbert spectrum calculated by three numerical probes of IWs at impermeable and permeable obstacles is presented in Figure 7. The transmitted wave energy of IWs in impermeable obstacles is also larger than that in permeable ones. A single fundamental frequency of IWs can be observed whether the IWs propagate over a trapezoidal obstacle with impermeable or permeable properties. Initially, the wave frequency is similar in impermeable or permeable obstacles (Figure 7a1 and b1). However, as the IWs propagate over the front slope of a trapezoidal obstacle, oscillations in wave frequency occur in the impermeable obstacle due to strong IWs-obstacle interactions and the internal hydraulic jump (Figure 7a2). In permeable obstacles, the wave frequency magnitude dissipates, and fewer oscillations are generated due to the weak internal hydraulic jump and porous

Marine Research of the National Academy of Marine Research
DOI: 10.29677/MR.202312_3(2).0005

interactions (Figure 7b2). When the IWs reach the plateau, the wave frequency magnitude dissipates significantly, regardless of whether the obstacle is impermeable or permeable (Figure 7a3 and b3). Comparing these results with those in Figure. 6 and 7, it is evident that the magnitude of SWs is stronger than that of IWs. This finding aligns with the earlier observed phenomenon of waveform evolution. In this paper, we examine the distinct evolutions of IWs and SWs propagating over impermeable and permeable trapezoidal obstacles, including wave amplitude, wave period, and flow field characteristics. When a system experiences periodic external forces or excitations, it can vibrate not only at the fundamental frequency, but also at frequencies that are multiples of the fundamental frequency, also known as harmonics. These harmonics include both integer multiples (such as 2 times the fundamental frequency, 3 times the fundamental frequency, and so on). These higher-order harmonics, occurring above the fundamental frequency, are known as supraharmonics. The propagation of IWs and SWs over impermeable and permeable trapezoidal obstacles leads to the occurrence of supraharmonics due to the nonlinear increase. This increasing component is caused by a nonlinear wave-wave interaction process with the wave energy transfer from the fundamental harmonic to the superharmonics.

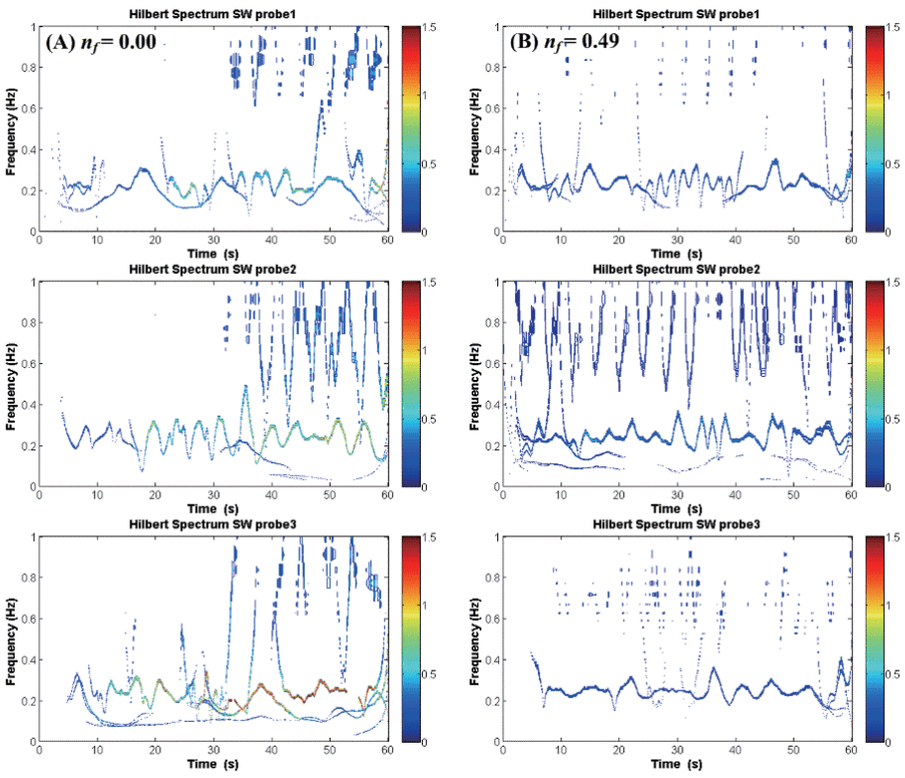

Figure 6. Time- frequency -energy pattern (Hilbert spectrum) calculated by HHT at three probe locations of the SWs along the wave flume. (Exp.: H_1 = 0.12 m, H_2 = 0.38 m; P_s = 40 rps; A: impermeable B: permeable, n_f =0.49)

Marine Research of the National Academy of Marine Research
DOI: 10.29677/MR.202312_3(2).0005

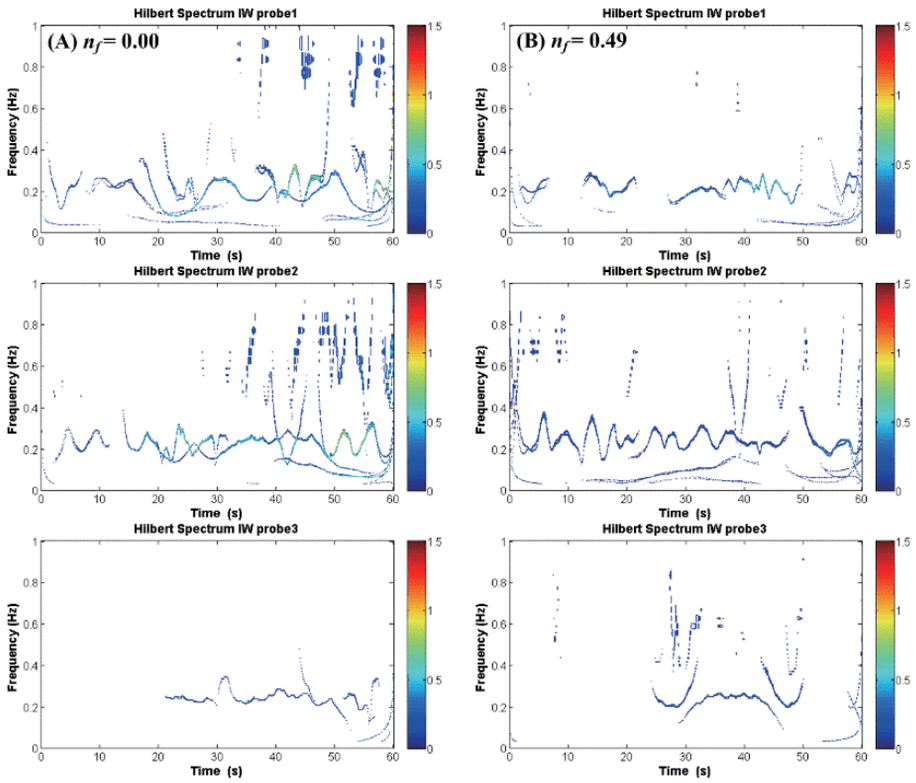

Figure 7. Time- frequency -energy pattern (Hilbert spectrum) calculated by HHT at three probe locations of the IWs along the wave flume. (Exp.: H_1 = 0.12 m, H_2 = 0.38 m; P_s = 40 rps; A: impermeable B: permeable, n_f =0.49)

The results from all time points in Figure 8 are aggregated to illustrate the variations in wave energy versus the characteristic frequency of SWs. In Figure 8, the vertical black dashed line represents the value of the wavemaker period (in R40, the repeated time is 4.5s). A fundamental frequency of the initial SWs is observed when the SWs propagate in deep water (Figure 8a1 and b1). However, as the SWs pass through the front slope and plateau, the fundamental frequency of SWs becomes significant due to IWs-obstacle interactions, particularly in the impermeable obstacle (Figure 8a2 and a3). In the case of the permeable obstacle, the fundamental frequency of the SWs maintains its original value as the SWs propagate over the submerged obstacle (Figure 8b1-b3). This reiterates that SWs' propagation under these conditions is primarily influenced by water viscosity. Overall, the fundamental frequency in the impermeable obstacle exhibits more oscillations, whereas that in the permeable obstacle remains constant during this process.

Marine Research of the National Academy of Marine Research
DOI: 10.29677/MR.202312_3(2).0005

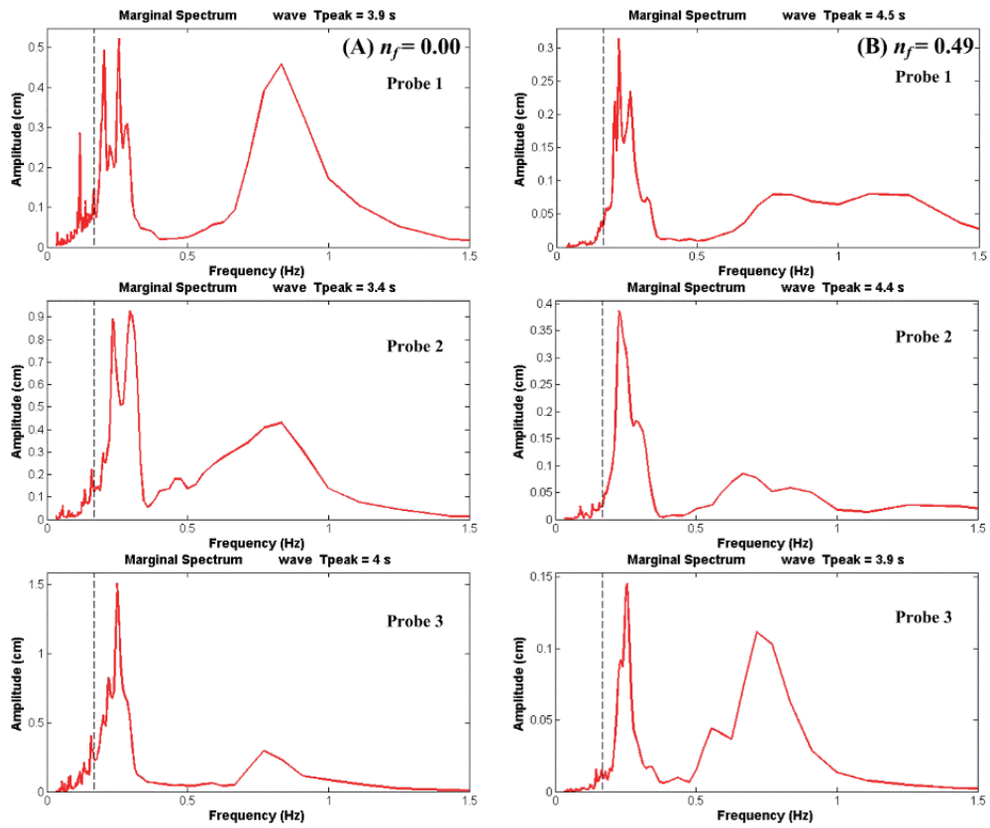

Figure 8. Variations of wave energy versus characteristic frequency at three probe locations of the SWs along the wave flume. (Exp.: H_1 = 0.12 m, H_2 = 0.38 m; P_s = 40 rps; A: impermeable B: permeable, n_f =0.49)

Using the same method, the evolution of wave energy versus the characteristic frequency of IWs is calculated and presented in Figure 9. The subplots reveal a significant dissipation of IWs' wave energy, whether the obstacle is impermeable or permeable (Figure 9). A fundamental frequency of the initial IWs is observed as the IWs propagate in deep water (Figure 9a1 and b1). When the IWs propagate on the front slope, the significant fundamental frequency of IWs is maintained in both cases (Figure 9a2 and b2), but it only causes oscillations in the impermeable obstacle due to strong IWs-obstacle interactions (Figure 9a2). As the IWs move onto the plateau, the strength of the fundamental frequency dissipates significantly due to the strong IWs-obstacle interactions in the case of the impermeable obstacle and the porous effect in the case of the permeable obstacle. In summary, the strength of the fundamental frequency of IWs in the case of the impermeable obstacle decreases significantly due to the internal hydraulic jump induced by trough-obstacle interactions when the wave propagates over a trapezoidal obstacle. A similar phenomenon is found in the case of the permeable obstacle due to the porous influence when the IWs encounter a trapezoidal obstacle.

DOI: 10.29677/MR.202312_3(2).0005

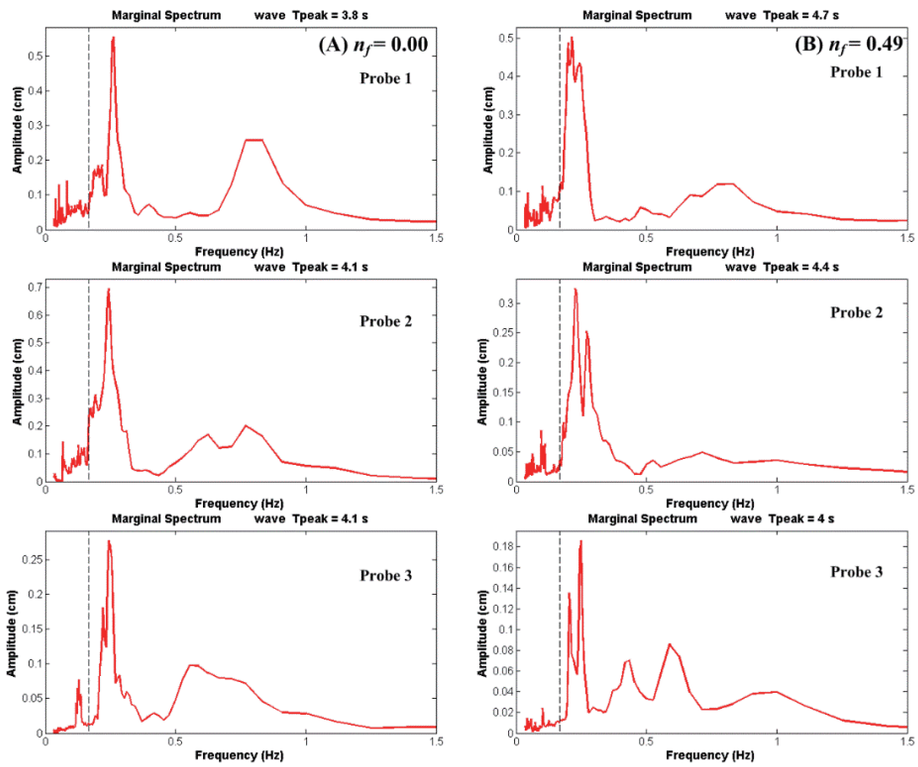

Figure 9. Variations of wave energy versus characteristic frequency at three probe locations of the IWs along the wave flume. (Exp.: H_1 = 0.12 m, H_2 = 0.38 m; P_s = 40 rps; A: impermeable B: permeable, n_f =0.49)

4 CONCLUSION

Using a plunger-type numerical wave maker, we conducted numerical simulations to investigate the interaction between IWs and SWs propagating over impermeable and permeable trapezoidal obstacles. The results indicate that the amplitude and wave period of SWs are influenced by the propagation of IWs over submerged obstacles. As both SWs and IWs pass through the trapezoidal obstacle, the wave amplitude decreases significantly, but the fundamental frequency remains constant regardless of whether the obstacle is impermeable or permeable. For impermeable obstacles, the strength of the fundamental wave period of IWs decreases as IWs propagate over the plateau. Additionally, oscillations can be observed in the Hilbert spectrum. Weak phenomena of internal hydraulic jump occur as IWs encounter the front slope. During this process, the fundamental frequency of SWs in the case of the impermeable obstacle induces more oscillations when SWs propagate over the trapezoidal obstacle. For permeable obstacles, the porous effect leads to a significant decrease in the amplitude and strength of the fundamental frequency of both SWs and IWs. The fundamental frequency of SWs in the case of the permeable obstacle remains constant and is only affected by water viscosity during this process. The strength of the fundamental frequency of IWs in the case of the permeable obstacle continuously decreases due to the porous influence when IWs encounter a trapezoidal obstacle.

ACKNOWLEDGEMENTS

The authors acknowledge the support from the Ministry of Science and Technology, Republic of China, grant No. MOST 109-2221-E-019 -029 -MY3.

DOI: 10.29677/MR.202312_3(2).0005

REFERENCES

Chen, H., Wang, Z., Cui, J., Xia, H., & Guo, W. (2023). Application of different internal solitary wave theories for SAR remote sensing inversion in the northern South China Sea. *Ocean Engineering, 283,* 115015. https://doi.org/10.1016/j.oceaneng.2023.115015

Cheng, M. H., Hsieh, C. M., & Hwang, R. R. (2020). Numerical study on the transformation of an internal solitary wave propagating across a vertical cylinder. *Applied Ocean Research, 95,*102016. https://doi.org/10.1016/j.apor.2019.102016

Dalziel, S. B., Carr, M., Sveen, J. K., & Davies, P. A. (2007). Simultaneous synthetic schlieren and PIV measurements for internal solitary waves. *Measurement Science & Technology, 18*(3), 533-547. https://doi.org/10.1088/0957-0233/18/3/001

Das, S., Sahoo, T., & Meylan, M. H. (2018). Flexural-gravity wave dynamics in two-layer fluid: blocking and dead water analogue. *Journal of Fluid Mechanics, 854,* 121-145. https://doi.org/10.1017/jfm.2018.617

Hao, X., Wu, J., Rogers, J. S., Fringer, O. B., & Shen, L. (2022). A high-order spectral method for effective simulation of surface waves interacting with an internal wave of large amplitude. *Ocean Modelling, 173,* 101996. https://doi.org/10.1016/j.ocemod.2022.101996

Ho, C. R., Su, F. C., Kuo, N. J., Tsao, C. C., & Zheng, Q. (2009). Internal wave observations in the northern South China Sea from satellite ocean color imagery. *OCEANS 2009-EUROPE, IEEE,* 1-5. https://doi.org/10.1109/OCEANSE.2009.5278324

Hsieh, C. M., Cheng, M. H., Sau, A., Hwang, R. R., Peng, Y. F., & Yang, W. C. (2019). Interaction between internal waves and surface waves over a slope-shelf [Conference presentation]. The 29th International Ocean and Polar Engineering Conference, Hawaii, USA. pp.3203-3210.

Huang, N. E., Shen, Z., Long, S. R., Wu, M. C., Shih, H. H., Zheng, Q., Yen, N. C., Tung, C. C., & Liu, H. H. (1998). The empirical mode decomposition and Hilbert spectrum for nonlinear and nonstationary time series analysis. *Proceedings: Mathematical, Physical and Engineering Sciences, 454*(1971), 903-995. http://www.jstor.org/stable/53161

Ko, D., & Cho, Y. (2017). A laboratory experiment on the surface and internal waves in two-layered fluids. *Ocean Engineering, 146,* 257-267. https://doi.org/10.1016/j.oceaneng.2017.09.060

McMullen, K. Y., Poppe, L. J., & Parker, C. E. (2015). Character, distribution, and ecological significance of storm wave-induced scour in Rhode Island Sound, USA. *Geo-Marine Letters, 35,* 135-44. https://doi.org/10.1007/s00367-014-0392-0

Shur, M. L., Spalart, P. R., Strelets, M. K., & Travin, A. K. (2008). A hybrid RANS-LES approach with delayed-DES and wall-modelled LES capabilities. *International journal of heat and fluid flow, 29*(6), 1638-1649. https://doi.org/10.1016/j.ijheatfluidflow.2008.07.001

Trowbridge, J. H, & Traykovski, P. (2015). Coupled dynamics of interfacial waves and bed forms in fluid muds over erodible seabeds in oscillatory flows. *Journal of Geophysical Research: Oceans, 120*(8), 5698-709. https://doi.org/10.1002/2015JC010872

Zhang, X., & Li, X. (2022). Satellite data-driven and knowledge-informed machine learning model for estimating global internal solitary wave speed. *Remote Sensing of Environment, 283,* 113328. https://doi.org/10.1016/j.rse.2022.113328

Zhang, J., Jiang, W., & Zhang, X. (2023). Analysis of a simplification strategy in a nonhydrostatic model for surface and internal wave problems. *Acta Oceanologica Sinica, 42*, 29-43. https://doi.org/10.1007/s13131-022-2068-3